Title:

Sensing Local Field Potentials with a Directional and Scalable Depth Array: DISC

Authors:

Amada Abrego Mancilla[1]†, Wasif Khan[1]†, Christopher E. Wright[1,2], Neela Prajapati[1], M. Rabiul Islam[1], Mohammad H. Ghajar[1], Xiaokang Bai[1], Nitin Tandon[1], John P. Seymour[1,3]*

Affiliations:

[1]Department of Neurosurgery, University of Texas Health Science Center, Houston, TX, 77030 USA

[2]Department of Bioengineering, Rice University, Houston, TX, 77030, USA

[3]Department of Electrical and Computer Engineering, Rice University, Houston, TX, 77030, USA

*Correspondence: John Seymour (john.p.seymour@uth.edu)

Abstract

A variety of electrophysiology tools are available to the neurosurgeon for diagnosis, functional therapy, and neural prosthetics. However, no tool can currently address these three critical recording needs: (i) a surgical method that can reach any cortical region in a minimally invasive manner; (ii) record microscale, mesoscale, and macroscale resolutions simultaneously; and (iii) enable recording from multiple brain regions. This work presents a novel device for recording local field potentials (LFPs) whose form is based on state-of-the-art stereo-electroencephalogram (sEEG). Using quasi-static electromagnetic modeling, the lead body is shown to shield LFP sources and this enables *di*rectional sensitivity and *sc*alability when microelectrodes are positioned radially, which we refer to as a DISC array. As predicted, DISC demonstrated significantly improved signal-to-noise, directional sensitivity, and decoding accuracy in the rat barrel cortex during whisker stimulation. Critically, DISC also demonstrated equivalent fidelity at the macroscale and, uniquely, performs current source density in stereo. Directional sensitivity of LFPs may significantly improve brain-computer interfaces and many diagnostic procedures, including epilepsy foci detection and deep brain targeting.

1. Introduction

For both clinical research and systems neuroscience, the question of recording scale in time and space is a fundamental and ongoing challenge. What spatial resolution is required to elucidate the etiology or diagnosis of this disease? Or what scale will best help us understand a systems neuroscience question? It is also a practical question of what measurement can be made. Clinicians typically choose non-invasive field potentials (electroencephalograms (EEG) and magnetoencephalograms (MEG)) to measure the health or dysfunction of electrical activity within the brain. When high spatial precision is also required, large area, subdural surface electrodes (a field potential known as electrocorticogram (ECoG)) and/or depth electrodes are used instead of EEG/MEG (Kovac et al. 2017). One of the most common intracranial recording procedures in humans occurs in drug-resistance epilepsy patients who present with potentially focal seizures. These procedures were once based on surface arrays (i.e., ECoG). Beginning in France in 1965 (Bancaud et al. 1965), slowly spreading in Europe, and finally being adopted in the U.S. in the last decade, ECoG recordings have been replaced with stereo-electroencephalogram (sEEG) (Engel 2018) for most diagnostic surgeries. sEEG is a specific form of depth electrodes typically with eight to sixteen ring electrodes. *Given modern pre-op imaging tools and frameless robotic guidance, its advantages over the ECoG grid are reduced hemorrhaging, infection, and migraines* (Tandon, Tong, Friedman, Johnson, Von Allmen, Thomas, Hope, Kalamangalam, Slater, and SA 2019; Yan et al. 2019; Sacino et al. 2019; Toth et al. 2019; Yang et al. 2017). Furthermore, there is less skull damage during the procedure, and significantly greater resolution in the measurement of signals not originating near the surface. These advantages have been impactful, for example, in the diagnosis of medial temporal lobe epilepsy. Resection surgery in one sEEG cohort resulted in 39% greater seizure freedom relative to ECoG grids (Tandon, Tong, Friedman, Johnson, Von Allmen, Thomas, Hope, Kalamangalam, Slater, and Thompson 2019). In short, stereotactic-guided depth arrays are an excellent form factor for minimally invasive delivery of electrodes to any brain region and enable large recording and stimulation coverage, addressing the need for interfacing large networks in the brain. The success of depth arrays suggests their use in more applications such as a brain-computer interface (BCI) although the decoding performance of the sEEG (Herff, Krusienski, and Kubben 2020; Angrick et al. 2020) is still trailing that of surface grids (Makin, Moses, and Chang 2020; Moses et al. 2021; Hammer et al. 2016) and the Utah array (Willett et al., n.d.; Thomas et al. 2020; Hochberg et al. 2012)(Willet; Crone; Hochberg). *As we will demonstrate, the sEEG in its current form is profoundly limited by the ring electrode, but a redesign of its electrodes has the potential to create a multi-scale tool for many applications.*

Besides field potentials, researchers have two other temporally precise recording domains: extracellular single cell (300-5000 Hz) and local field potentials (< 300Hz). The former is generally

preferred in systems neuroscience and BCI but produce currents only measurable within 100-120 μm of the source (Du, Roukes, and Masmanidis 2009). This limits the volume of brain tissue one can measure. Local field potentials, which imply the use of microelectrodes, are generally viewed as providing a spatial resolution between the field potential and single cells. It has been shown that local field potentials are recorded from far-reaching sources, as well as the adjacent cellular structures (Lindén et al. 2011), and therefore suffer from the “cocktail party” problem. Relative to spiking single cells, the LFP has poor fidelity and an ill-defined waveform. It is well understood that many simultaneous sources, and limited signal-to-noise ratio (SNR) and directional information make source separation challenging. Source separation algorithms continue to be a highly active area of research (Oosugi et al. 2017; Lucka et al. 2012). So for researchers and clinicians, the choice between extracellular recordings versus LFPs is complicated by insertion techniques, but certainly includes a tradeoff of signal fidelity and the volume of tissue measured.

Exactly what details are measurable from FPs and LFPs is an ongoing question and a function of the electrode and device geometry, and the distance from the source (Pesaran et al. 2018; Lindén et al. 2011; Kajikawa and Schroeder 2015). The largest signals are driven by the synaptic transmembrane current in populations of neurons whose geometry most strongly approximates an open-field dipole (Nunez and Srinivasan 2006; Buzsáki, Anastassiou, and Koch 2012). Layer V neurons throughout the mammalian neocortex are the best example of this and have been demonstrated in biophysical models to accurately account for microelectrode-based LFP recordings (Hagen et al. 2018; Dura-Bernal et al. 2019), and EEG and MEG signals (Neymotin et al. 2020; Næss et al. 2021). As predicted, the LFP from even a small, localized source can travel 6 mm before it is attenuated 50%, as demonstrated in macaques (Kajikawa and Schroeder 2011). Critically, the arriving information at a microwire, for example, does not contain directional information, although it could be triangulated if the spatial spread of an array of microwires and SNR was sufficient. Source separation, and the harder problem of localization, work best with spatial diversity of electrodes. Nonintuitively, microelectrodes are more susceptible than macroelectrodes to the cocktail party problem because, unlike large ring electrodes, these remain highly sensitive to the diverse, local, and laminar sources of the immediate cortical column (Herreras 2016). Conversely, a ring macro-electrode is effectively the weighted sum of all voltage contributions across its surface (all 360 degrees) and this greatly attenuates the local input. To summarize, this inability to conduct source separation effectively for LFPs limits its usefulness in neuroscience, neurology, and brain-computer interfaces (BCIs), especially confounding our resolution in the mesoscale – 0.1 to 5 mm.

This report describes a novel multi-scale recording array capable of stereo-LFP and current source density measurements. The *di*rectional and *sc*alable array, which we simply refer to as DISC, is intended to offer an improved mesoscale range. We will contrast DISC with tetrodes and virtual ring electrodes. This work uses a finite element model based on electro-quasistatic physics and an acute *in vivo* demonstration in the rat barrel cortex, which is chosen for its simplicity in creating spatially disparate neural activity. The directionality and mesoscale decoding achieved here was made possible with insertion through a small twist-drill hole similar to the sEEG procedure which takes only several minutes in humans (Rollo et al. 2021). An under-appreciated phenomenon, which we refer to as "substrate shielding", is quantified in the context of LFPs. Others before us were the first to identify the phenomenon but on a smaller scale. Two reports (Anderson, Oweiss, and Bierer 2001; Moffitt and McIntyre 2005), and later others and ourselves (Seymour et al. 2011) describe how neurons can be shielded by the device, resulting in directional sensitivity. Since that work, Boston Scientific has begun offering directional electrodes in the form of a ring with 3 segmented sections across a 1.2 mm diameter DBS lead body. Recently, detailed modeling by Noor and McIntyre (Noor and Mcintyre 2021) describes the quantitative advantages of the segmented electrodes versus ring electrodes in providing directionality. This report expands these concepts in a more generalizable design and establishes why microelectrodes on larger substrates may be transformative to neuroscience and clinical diagnosis. We quantitatively describe the variables of substrate diameter, electrode size, source orientation, and distance. We demonstrate a tool capable of high quality, multidirectional CSD, mesoscale source separation, and ring-equivalent recordings. Finally, we describe several manufacturing approaches for making DISC in a way that is compatible with the goal of stereotactic-guided insertion of depth arrays.

2. Results

2.1 Electro-quasistatic model of substrate shielding and directional sensitivity

As previously described by others, Maxwell's equations can be reduced to an electro-quasistatic model with the current conservation law applied to an array of sinks and sources in the extracellular space of the brain (Hämäläinen et al. 1993; Baillet, Mosher, and Leahy 2001). These results apply to all frequencies of clinically relevant extracellular potentials. The Poisson equation,

$$\nabla \cdot \mathbf{J} = \nabla \cdot (\sigma \nabla \phi) \,, \quad \text{(eq. 1)}$$

where J is current density, σ is conductivity, and ϕ represents the extracellular electric potential, can be applied to arbitrary current sources in a conducting volume with boundary conditions including the insulating body of a recording device. The FEM package ANSYS was used throughout this study to model a variety of current sources and device geometries.

Directionality as a function of substrate diameter

To compare microwire, ring electrode, and the **di**rectional and **sc**alable (DISC) array, we modeled a dipole approximating a cortical column from layer V pyramidal cells (1.2-mm height and 1.67-A/m^2 current density) (Murakami and Okada 2015) (Fig. 1). Later, we model a variety of other sources, orientations, and distances to illustrate the range of this effect. A useful measure for the "directionality" of a source and device combination is the change in voltage between nearby electrodes. Directionality is conveyed as the front voltage to back voltage ratio (F/B), which is shown to be dominated by substrate diameter. The normal declination of voltage should be between 1/r and 1/r^2 depending on the geometry of the sources, but the F/B ratio is significantly higher than expected or previously reported and grows nonlinearly with the diameter (Fig. 1C). Large diameter insulating bodies create a disturbance in the voltage contours unlike smaller single unit recording tools (e.g. Benke-Fried wires (Fried et al. 1999), IMEC probe (Jun et al. 2017), Utah array, or microwires). Since this demonstration also creates an increasing distance between electrode pairs, it is important to compare this ratio when the lead body conductivity matches the value of tissue (σ=0.276 S/m) (Fig. 1C green line). The difference demonstrates the effect of "substrate shielding" for a significant LFP source, which is caused by the elongated path current must take to reach lower potentials. Current flow in this model near the insulating body is demonstrated in Suppl. Fig. 1, which illustrates why the isopotential around the front electrode extends toward the source, and the isopotential around the back electrode extends away from the source. These combined effects provide a previously undescribed directionality available to a larger diameter device when recording field potentials from synchronous sources even at considerable distances.

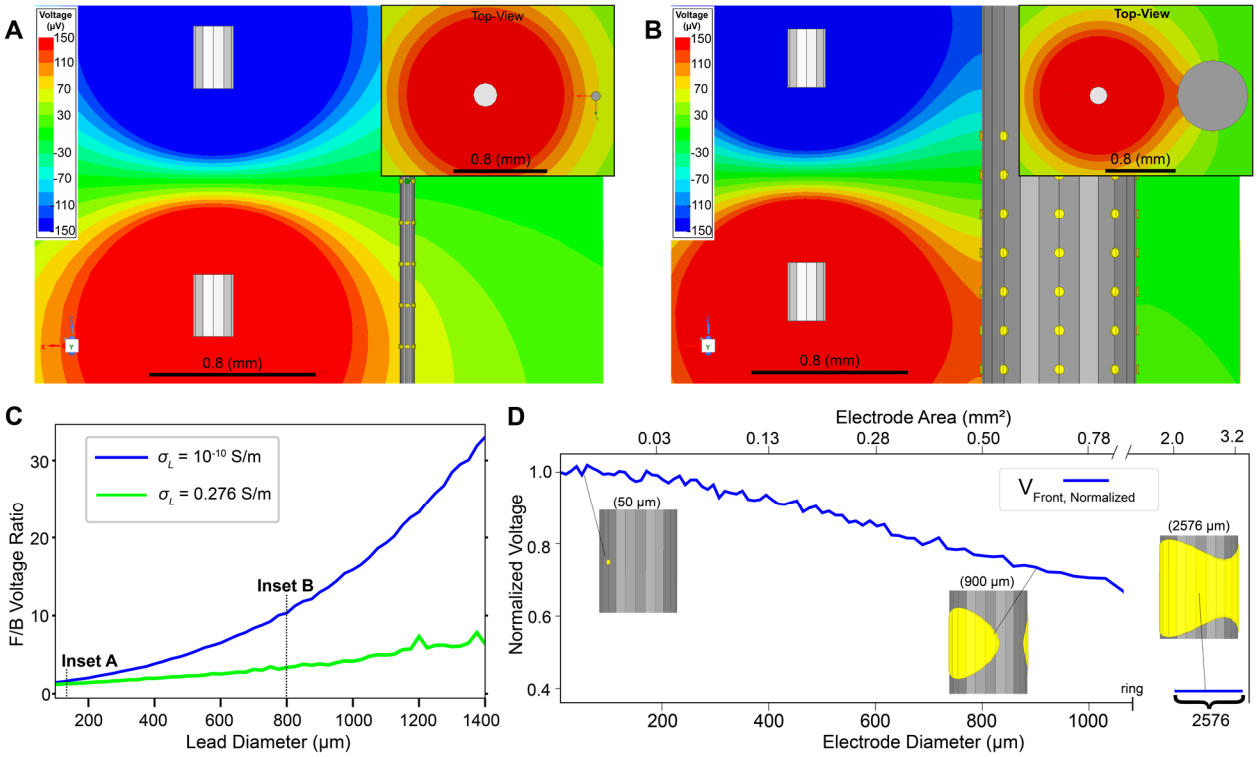

Figure 1. **Directionality and amplitude as a function of substrate and electrode diameters. A,** A 65-µm diameter and **B,** 800-µm diameter substrate with an electrode on opposite sides at a fixed gap from a dipole source. All electrodes are independent (not touching). Voltage V results from the current source shown to left of the lead body representing layer V pyramidal cells in the rat cortex (200-µm diameter) created in a finite element model (ANSYS). Voltage is inversely related to distance and perturbed by changes in conductivity σ in space such as created by the insulating body. **C,** ANSYS model of the front to back electrode voltage ratio as a function of diameter ($Ø_{sh}$). When σ of the lead body matches local tissue (σ=0.276 S/m), F/B increases due to the increasing distance between front and back electrodes. Substrate shielding magnifies the difference between the front and back electrodes. **D,** Normalized voltage amplitude as a function of electrode diameter. The source was identical as before. Attenuation becomes significant beyond 120 µm. At 1238 µm, a ring forms (e.g., sEEG) and amplitude is attenuated by 60% relative to a microelectrode. Increasing the ring area beyond this point has negligible attenuation. A video of this effect may be found in Suppl. Movie 1.

Electrode diameter and LFP source amplitude

Large electrode area is likely to be most practical in noisy clinical environments given the low impedance and therefore poor EMI pickup. We parameterize the electrode diameter on a 800-μm lead body and measure the peak amplitude when a dipole and the nearest electrode have a gap of 0.8 mm. The decline in amplitude with increasing diameter (or area) is quite significant even before the electrode wraps around the substrate to form a ring (Fig. 1D). Once the ring forms, the area no longer has any significant affect. A 120-μm diameter microelectrode (11,300 μm^2) has only a theoretical loss of amplitude of 3% for dipole-equivalent LFP sources. A minor attenuation may be an excellent tradeoff given some degree of EMI and thermal noise immunity, and therefore achieve greater SNR. An important comparison is the Boston Scientific directional lead which has an electrode width of 1 mm. This model predicts that a 1-mm diameter electrode will be attenuated by 27% relative to even a 120-μm electrode (their actual lead is a 1.5-mm tall rectangle, so the difference is likely greater).

Source geometry and orientation

The model so far considered an orientation most likely encountered when the array implantation is normal to the neocortical surface and parallel to cortical columns. Many device trajectories (Vakharia et al. 2017; Rollo et al. 2021) and therefore dipole orientations are possible. Open field dipoles may also appear as local sinks or sources (monopoles) and represent the best-case attenuation (~1/r). Each of these situations can create a different directional sensitivity (i.e. F/B ratio) and attenuation profile. While not exhaustive, we analyzed a monopole (200 μm), dipole (200 μm), large dipole (700 μm), and orthogonal dipole all at varying distances in the range of 0.15 mm to what Nunez et al. define as the mesoscale, up to 5 mm (Nunez, Nunez, and Srinivasan 2019). The F/B ratio over distance for each is a useful quantitative juxtaposition. As expected, a parallel-oriented dipole has the greatest directionality but the least range (3dB distance equals 1.9 mm). The monopole and orthogonal dipole performed similarly with a 3dB distance equal to 4.0 mm) (Suppl. Fig. 2, Suppl. Movie 2).

Directionality in a noisy multi-source environment

In another model, we introduced eight cortical sources within ~5 mm of the devices (Fig. 2), added thermal noise at each electrode, and measured the SNR during an evoked potential task attempting to isolate each source based on phase (see *Methods*). The amplification of the voltage from a dipole with its nearest electrode is direction dependent, meaning any source from a

significantly different angle is attenuated by some degree and thereby reducing the biological noise. Our simulation provides for a challenging scenario by varying distance and diameter dramatically (Fig. 2A, B, Suppl. Table 2). Source 1 for example has two other sources within 20 degrees and therefore communicating over the same column of electrodes. Similarly, source 3 and 4, and 5 and 6 have similar angles. Source 1 at 1 mm has an SNR = 1.8 dB with no repeated trials and 7.6 dB after 50 trials (Fig. 2C). For an ultra-high-resolution ring electrode (0.4-mm tall, 0.8-mm diameter) the SNR was 0.38 and 3.9 dB. Note that 2-mm tall ring electrodes are standard and these would have performed considerably worse given the narrow peak of voltage from a dipole (Fig. 1). This difference exists despite the addition of a 4.3 μVrms (root mean square) on DISC microelectrodes, whereas the ring electrode included only 2.7μVrms. DISC does not always have lower noise (data not shown) but does have greater SNR for each of the 8 sources. The most distant sources, except the large source 7, had relatively modest improvement for DISC in this source configuration. CAR improves SNR for the farthest sources by subtracting out biological background noise. The ring electrode outperforms a microwire for all but the closest source because of its lower noise floor. Arrays of microelectrodes would have also benefited from CAR (Ludwig et al. 2009) although not tested here.

Virtual electrode geometries can be computed with digital averaging and referencing (Blanche et al. 2005). Generating an equivalent macroelectrode signal is important because of its long clinical history and effective filtering in certain frequencies (Nunez and Srinivasan 2010). We validate this ability theoretically using ANSYS and the previously described multi-source and noise simulation model. For each of the 8 sources in our model, we measured both the ring and virtual ring (comprised of 3 x 8 electrodes at the same depth) and found DISC performed nearly equivalently across sources (Suppl. Fig. 3).

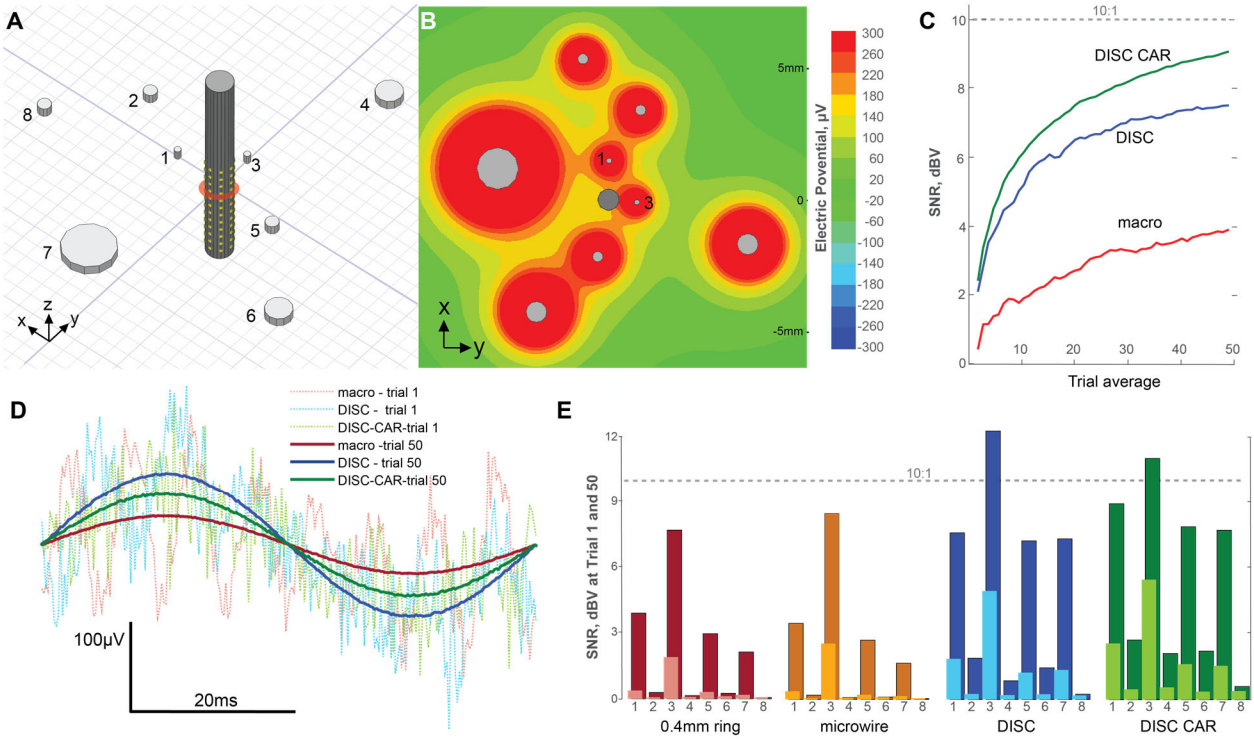

Figure 2. **Electro-quasistatic 3D dipole model demonstrating directional sensitivity in a multi-source configuration. A,** 8 simultaneous dipoles modeled in FEM with identical surface boundary current density (only sink is shown, 0.5-mm grid). Three device types are modeled—DISC (shown), microwire, and 0.4-mm tall ring electrode. **B,** Voltage heat map through layer V dipoles with sources on at peak current (1.67×10^3 nA/mm^2). Heat map is at the plane intersecting the dipole sinks. **C,** Signal-to-noise (dBV) for macro, DISC, and DISC with CAR during trial 1 and cumulative trials. **D,** Waveform examples for 1 and 50 trials for the macro and DISC electrode when phase locked to Source 1. Sources 2-8 are assigned a random phase and frequency. Assigned noise of 2.7 μVrms and 4.3μV to each ring or microelectrode, respectively. **E,** SNR comparison of the simulated potentials for each source independently phase-locked. Microwire Ø=65μm. Trial 1 = light color; Trial 50 = dark color (avg).

2.2 In vivo amplitude, SNR, and directional sensitivity

Amplitude and SNR

One tetrode (50-μm bundle diameter) was implanted into 7 rats each with 9 whiskers being stimulated over 450 trials. Immediately following the tetrode recordings, DISC was implanted into

the same 0.9-mm twist drill hole on the identical trajectory (typically 38° relative to the sagittal plane). A small twist drill hole was critical to reduce brain dimpling. DISC has 128-channels of 80-µm electrodes wrapped on a rigid cylinder (650-720-µm diameter) and implanted 3.2 mm until the top electrode row was no longer visible (details in *Methods*). We compare the tetrode, DISC, and two virtual ring electrodes. One ring type was a 0.4-mm tall x 3 array and the other a 2-mm tall single electrode (a commercial standard). The 0.4-mm rings spanned infragranular, granular, and supragranular layers. The mean amplitude of the LFP signal of our DISC device (254 ± 198 µV) was significantly better than the tetrode (80 ± 70 µV, Tukey's test $p<0.001$), virtual 0.4-mm ring (129 ± 108 µV, $p<0.001$), and the virtual 2-mm ring (64 ± 70 µV, $p<0.001$). Similarly, the DISC device significantly improved the LFP SNR (dBV) (DISC: 13 ± 3, tetrode: 8 ± 4 virtual 0.4-mm ring: 10 ± 4, virtual 2-mm ring: 7 ± 4, $p<0.001$) (Fig. 3). The mean rms noise floor across subjects was 4.3 ± 1.6 and 4.7 ± 1.1 µVrms (100ms window prior to stimulus) for DISC and tetrodes, respectively. In practice, CAR improved the SNR(dBV) in trial averages, increasing it by 2 to 15 ± 3 dBV (Tukey's test, $p=0.001$). A lower amplitude was also noted for CAR (Suppl. Fig. 4), as expected from theory. All experiments were recorded in a Faraday cage. To illustrate noise immunity with CAR, we also recorded a session with an intentional ground loop and no Faraday cage, which in this example made an significant, observable difference (Suppl. Fig. 5).

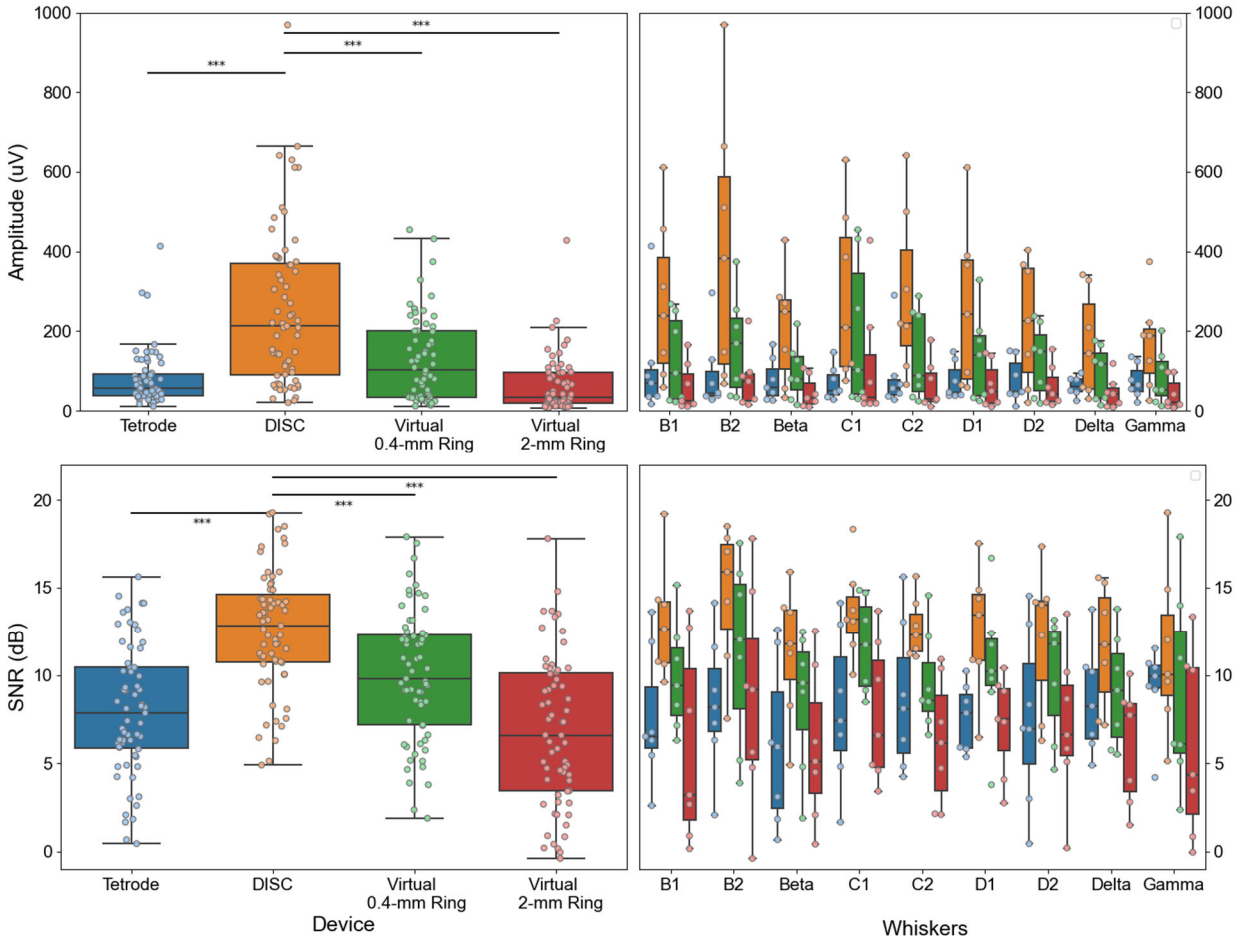

Figure 3. Amplitude and SNR for each device type. Ring electrodes were created virtually by averaging over a virtual ring of height 0.4 mm or 2 mm. Vertical pitch of DISC array was 200 µm. Whisker by whisker values are shown to the right. N=7 subjects and 9 whiskers each.

Directional Sensitivity and CSD

Cytochrome staining was performed in some subjects to identify the device location. Histology from subject S6 indicated DISC and the microwire were implanted in barrel E1 (medial edge of barrel field). A directional voltage profile (detailed in *Methods*) for nine whisker stimuli also correlated to the position identified in histology (Fig. 4, Suppl. Fig. 6). We also modeled dipoles at the specific histological coordinates and diameter for each of nine barrels and plot the FEM predicted profiles (Fig. 4C). Our model assumed a perfectly confined excitation pattern instead of the expected lateral excitation between barrels (Petersen 2019; Peron et al. 2015), which would at least partially explain the broad profiles found *in vivo* relative to FEM. Directional profiles

showed greater variance from trial to trial, as expected given independent electrode noise. Examples of the resultant vector measurement are provided for 3 subjects (Suppl. Fig. 7).

Results for local circuit measurements are still important especially in systems neuroscience. In several subjects with a known barrel location, we performed CSD analysis to evaluate its ability to conduct stereo-CSD measurements. CSD is a solution to equation [1] given known potential values across the lamina (Buzsáki, Anastassiou, and Koch 2012). The results demonstrate CSD from two opposing direction in an example using barrels D1 and gamma (Fig. 4D).

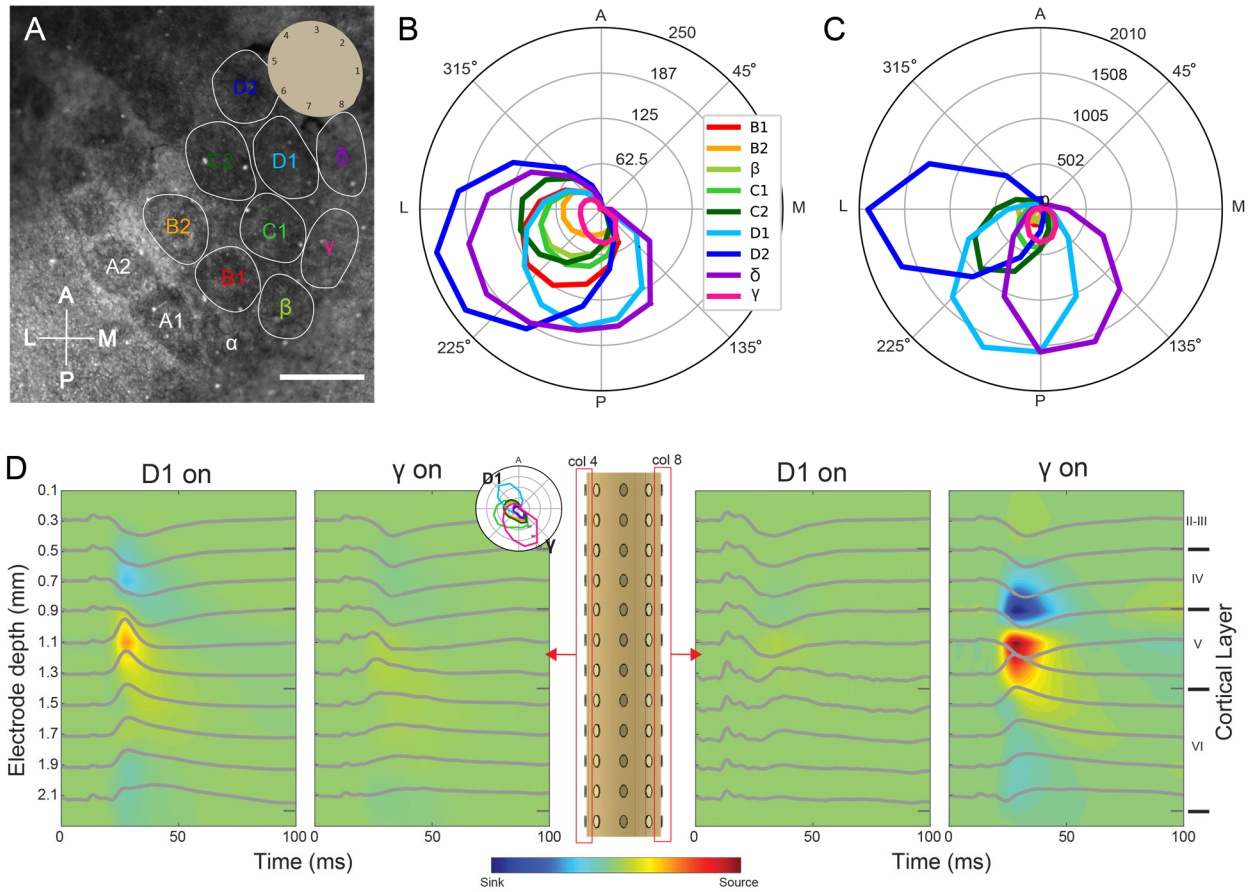

Figure 4. Demonstrating the directional sensitivity in rat barrel cortex. A, Example histology results using subject S6 and electrode layout from device 3. Unedited histology in Suppl. Fig. 6. Scale = 500 µm. **B,** LFP data from subject S6 and nine whiskers (depth=1.2mm). Directional polar plot formed from 8 channels, interpolated to 16 channels (~22.5°), and subtracted the minimum amplitude. **C,** FEM results assuming nine dipole sources spaced in an identical location as shown in the cytochrome-stained image. **D,** Multi-directional CSD from DISC demonstrated in subject S7 when two independent primary whiskers are stimulated. Barrel D1 was located closest to device

column 4 while barrel γ was located on column 8 (~180°). Polar plot of all whiskers shown in inset. Distinct CSD amplitude attenuation is observed. Average from 450 trials.

2.3 Whisker decoding and information capacity

Using the whisker stimulation experiment described above, we tested the accuracy of each device type in a 9-class discrimination task (Fig. 5). Our basic feature matrix prior to principal component analysis (PCA) consisted of the gamma band waveform (0:0.5:100ms) for each included electrode. Each row represented one trial. PCA was applied for dimensionality reduction before classification. Linear discriminate analysis and 10-fold cross-validation was performed for all classifications.

DISC accuracy when using 11 rows and 4 columns was an average of 93.0 ± 2.9% and was significantly better than the tetrode, 0.4-mm x 3 ring array, and the 2-mm ring (Fig. 6, Suppl. Table 1). The 3-ring virtual device performed second best, and was significantly better than one 2mm ring, which is the size of a standard sEEG. Each subject was analyzed independently where subject ID was a random effect in our generalized linear mixed model.

The classification accuracy of different electrode configurations and devices were tested and summarized in Suppl. Table 1. The best electrode configuration was 11 rows x 8 columns, but the 11 x 4 configuration was not significantly different and thus used in the device comparisons (Fig. 6). Overall, the electrode configuration provided the strongest influence on DISC accuracy. Classifying with more than 11x8 channels has not yet been attempted. The 11 rows selected were in layers I to VI and the 4 columns were alternating to reduce redundancy.

An important contrast is the DISC 1x4 configuration with the tetrode to separate out the affect of channel count. We chose 4 orthogonal electrodes on DISC in the same layer as the implanted tetrodes (1.4 mm deep). DISC significantly outperformed the tetrode with an accuracy of 68.3 vs 48.2% ($p<0.001$). The amplification and substrate shielding affects can best explain this performance (Fig. 3).

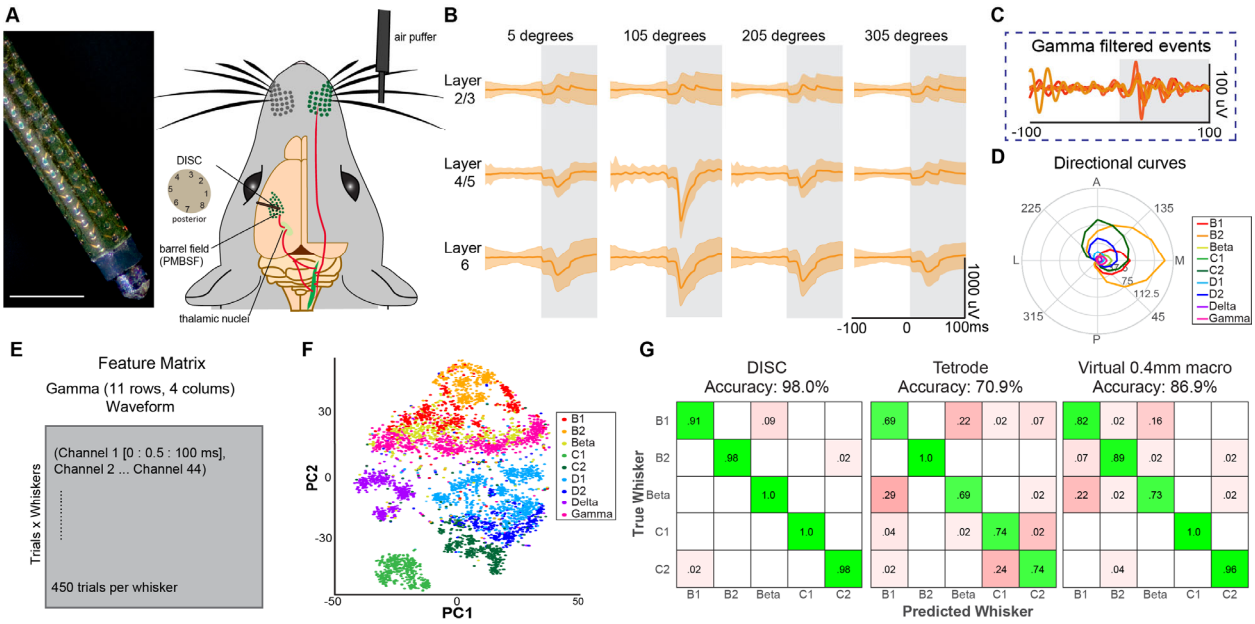

Figure 5. Methods and feature engineering overview for whisker stimulus discrimination. **A,** Experimental design and DISC image. Scale = 1 mm. **B,** Example 3x4 arrangement demonstrating evoked response across four directions for subject S4. **C,** Example of gamma filtered response. **D,** Polar plot of 9 whiskers (amplitude and direction). **E,** Feature matrix arrangement. **F,** Dimensionality reduction and source separation using PCA. **G,** Example confusion matrix for three device types after analysis with a linear discriminant analysis (LDA) model.

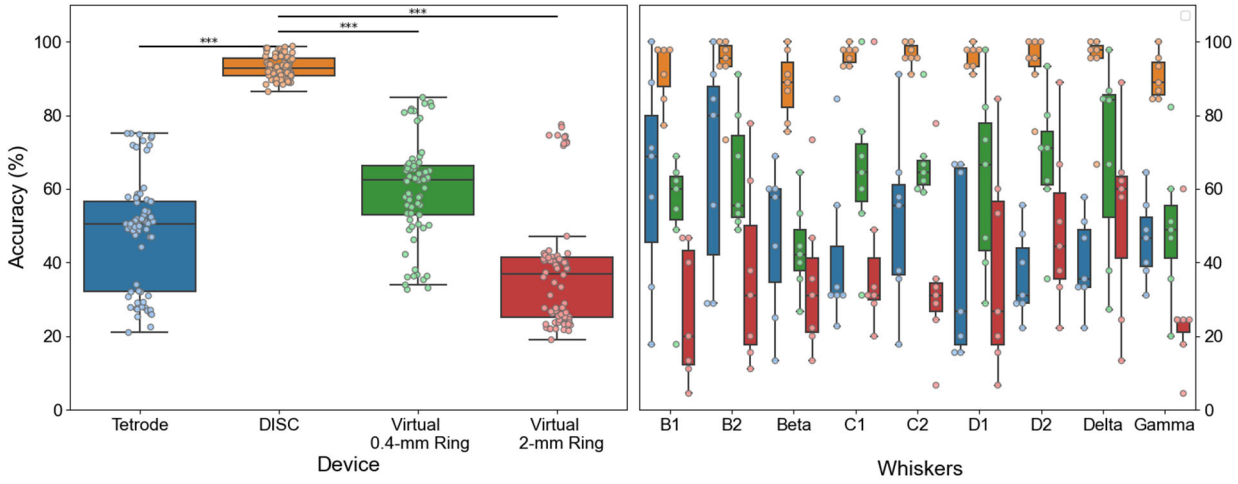

Figure 6. Decoding accuracy for each device type using a linear discriminant analysis model. (*** denotes p<0.001, generalized mixed effects model, 7 subjects, 10-fold cross-validation). Whisker by whisker values are shown to the right,

2.4 DISC manufacturing

A variety of manufacturing methods were tested and conceived to improve the likelihood of translation. Prototype linear arrays were manufactured in our cleanroom at Rice University using a polyimide-metal-polyimide process as previously described (Na et al.), but this resulted in poor axial alignment and complicates the backend design (Fig. 7A, backend not shown). Next we purchased similarly manufactured arrays from a commercial source originally designed for high-density ECoG (Diagnostic Biochips, Inc) and used an assembly technique previously described (Pothof et al. 2016)(Fig. 7B). The first challenging aspect of this method is the tolerance in mold and device manufacturing makes fitting parts difficult. Also, if epoxy is used, the needed tight tolerance creates large capillary forces and often coats electrodes during the curing process. Another assembly approach is wrapping the array using heatshrink (details in *Methods*). Pattern a thin (20 μm) adhesive sheet and mount on the backside of the 128-channel array. Prepare an insulated stainless-steel wire (432-μm diameter). Wrap the components using heat shrink and heat gun (Fig. 7C). This provided the greatest electrode yield and un-altered impedance values. There are many future options including wrapping on a silicone cylinder, direct molding of the PI array, and additive manufacturing.

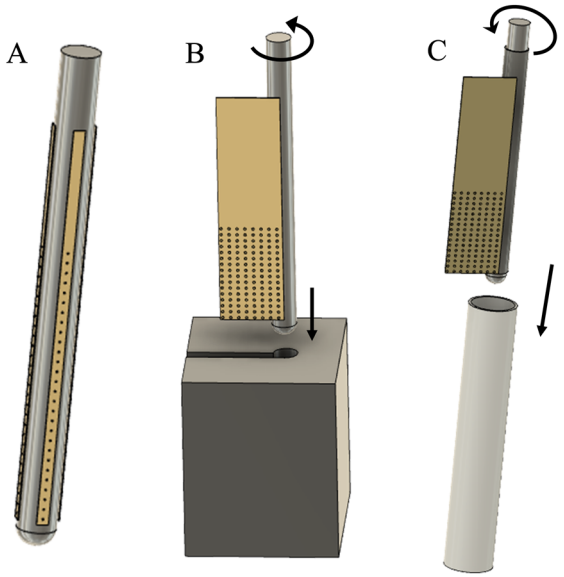

Figure 7. Example fabrication and assembly schematics available to practitioners. A, Linear polyimide arrays attached to rigid cylinder. **B,** Wrapping onto a rigid cylinder inside a rigid mold (originally proposed by (Pothof et al. 2016)). **C,** Wrapping method over a rigid body using heatshrink became our preferred method.

Discussion

Critically, DISC was effective at the whisker classification task at range despite its relatively narrow footprint. As predicted by the Shannon-Hartley theorem, the channels on DISC had higher SNR (Fig. 3) and thus the capacity to carry more information (Shannon 1948). This is supported by the virtual DISC-tetrode performance against the very small real tetrode. Also, in subject S6, the furthest barrel was 1.42 mm away (β). The accuracy of this subject remained very high despite the barrel distance (92-100%, 10-fold cross-validation, Suppl. Fig. 6). The spatial diversity of DISC provides a unique advantage relative to the other tested devices and yet it did not require a large craniotomy as would be necessary for a Utah array or an ECoG array. Like DISC, the virtual 0.4-mm ring array had unique layer information that likely contributed to its high accuracy. Unlike the other device types, DISC has directional information. The vertical span and the directionality are the most likely factors enabling decoding success. Having more electrodes, despite their redundancy, also proved to contribute significantly (Suppl. Table 1). This redundancy may have effectively denoised some part of the trial-by-trial noise. No trials were removed in any analysis.

Our results demonstrated for the first time, as far as we are aware, multi-directional CSD recordings. This capability may, for example, contribute to the understanding of lateral excitation or inhibition between cortical columns (Kato, Asinof, and Isaacson 2017). Encapsulation tissue may attenuate CSD results in chronic applications, which should be investigated. While many in the field cite a causal relation between encapsulation thickness and signal attenuation, the only published model on this topic (Moffitt 2005) predicts a complicated relationship even at the microscale. The local cortical columns will likely be damaged, but in a recent histological study around an 800-μm sEEG (N=3 devices), the measured radius of tissue damage in a non-human primate was only 50 μm for neuron density and 100 μm for astrocyte reactivity (Gerbella et al. 2021). This is more damage than expected from most neuroscience tools such as a tetrode, silicon microelectrode, and especially fine, flexible single cell tools like the NET probe (Luan et al. 2017). For DISC the goal is to record LFPs which are known to be more stable in chronic applications than single units, at least with a Utah array (Perge et al. 2014; Flint et al. 2013). Given their well-established distance of communication, only the most local LFP sources should be

affected. Future work should conduct long-term recordings but also explore the parameters of resistivity and thickness inside of a more detailed biophysics/FEM model. We also do not suggest the use of DISC in mice given the lack of usefulness from other large devices such as a U-probe (300-μm diameter). The small twist-drill hole we use (0.9 mm) may be an important factor for its success in rats.

Another advantage of DISC is its interchangeability with the stereo-EEG depth array, which has high placement accuracy (Vakharia et al. 2017), greater efficacy, and safety relative to grid arrays as reviewed earlier in the context of focal seizure detection. No studies exist comparing sEEG with the Utah array, but several comparisons are worth noting. Thousands of epilepsy patients receive 10-20 sEEG devices each year for typically 1-2 weeks (Kaiboriboon et al. 2015). In one study reviewing 150 procedures, the robotic sEEG surgery averaged 81 minutes and 6.2 minutes per electrode (Rollo et al. 2021). The average surgery in this review implanted 13 sEEGs, having an insertion angle of 0-75° with no significant change in registration accuracy based on angle. By contrast, the Utah array has only been implanted in approximately 21 persons with 1-6 implants each (Bullard et al. 2020). A single Utah array requires approximately 20-100-mm diameter skull opening for insertion, but the craniotomy size and surgical duration are not well published. The cumulative neurosurgical experience and exceptionally low infection and hemorrhage rate when using sEEGs offer a safety advantage to non-stereotactic approaches (Herff, Krusienski, and Kubben 2020). As further evidence of the low risk of twist drill implants, they are commonly used to relieve pressure in chronic subdural hematoma and are performed at the bedside with local anesthesia only (Xu et al. 2018; Hanalioglu et al. 2020).

It is interesting to note that the popular U-probe (Ulbert et al. 2001) can be viewed as a smaller version of DISC with a one-sided column of microelectrodes. The effect of substrate shielding is still measurable even at 300um (Fig. 1C). Substrate shielding predicts that this lead body will attenuate many biological sources while amplifying those in the direction of the single column of microelectrodes. This laminar arrangement is ideal for CSD and its stereotactic insertion is several reasons for its usefulness in macaque models. DISC is the generalization of this concept and will provide similar benefits but at a greater scale and in multiple directions (Fig. 4).

Given we did not have access to a silicone cylinder of the right diameter, we used a stainless steel (SS316) core. A silicone- or polyurethane-molded cylinder would provide greater flexibility and that might result in greater signal stability in long-term applications (Wellman et al. 2017). Future work should include advanced manufacturing methods to improve flexibility, including

wrapping on a silicone molded core followed by laser cutting of the polyimide to generate a mesh with less stiffness.

Conclusions

This work demonstrates a highly effective, compact tool for improving amplitude, SNR, and decoding accuracy in a whisker decoding task. The decoding performance was due in part to the directional sensitivity that generated greater diversity of signals across the narrow array. The *in vivo* demonstration agreed well with the predictions of the electro-quasistatic model, despite the potential for local damage of DISC relative to a much smaller tetrode. These results also demonstrated accurate source separation and to a smaller degree, source localization (Fig. 4). More research is needed to demonstrate the source localization accuracy, especially for sources beyond a few millimeters. Two or more DISC arrays in tissue may be highly effective in future work and would benefit from finite element software like Brainstorm (Tadel et al. 2011). We will continue to improve the manufacturability of DISC and demonstrate its diagnostic capability in epilepsy models and advanced decoding tasks. We hope this work encourages the field to accelerate the trend toward smaller ring electrodes, directional leads, and ultimately toward high-density circular (DISC-like) arrays to explore the impact of LFPs “in stereo” and multi-scale.

Methods

1. Modeling and simulation

ANSYS Electronics Desktop 2021 R1 with the DC Conduction module was used throughout this work. A tissue block was modeled as 14 x 14 x 14 mm^3, σ_{tissue} = 0.26 S/m, ε_{tissue}= 80 (Koessler et al. 2017). Lead substrate was 6-mm tall and a variable diameter, $Ø_{sh}$, between 10 and 1400 microns. DISC diameter was by default 0.8 mm to emulate a standard sEEG device. σ_{shaft} = 1e-10 S/m. ε_{shaft}=2.7. Cortical monopoles and dipoles had identical properties as tissue. A uniform current density of I_d = 1.67x10^3 nA/mm^2 was applied to the surface of all sources, which was derived from the work of Murakami and Okada demonstrating an invariant dipole current across animals of Q = 1-2 nAm/mm^2 , where $Q = I_d \times d$ (Murakami and Okada 2015). We chose Q = 2 nAm/mm^2 and a dipole distance, d, of 1.2-mm center to center. Unless otherwise stated, the dipole diameter was 200 µm. All microelectrodes and ring electrodes were platinum, σ_{Pt}= 9.3e6 S/m.

The ring electrode was 0.4 mm tall. Three contiguous surfaces of the tissue block outer surfaces were defined as 0V to emulate a distant reference.

Figure 2 demonstrated 8 unique sources spread radially using an arrangement shown in Fig. 2A,B with details in Supplemental Table 2. That arrangement was intended to capture micro-, meso-, and macroscale sources interacting within a range of 5.1 mm in all directions. Sources 1, 2, and 8, and separately 3 and 4 had overlapping angular positions and therefore used the same electrode column for best amplitude. For each trial, one primary source was assigned a phase, φ=0π, and freq, *f*=16.67 Hz, while the other 7 sources a randomly assigned a random phase (0π to 2π) and frequency (40 Hz to 150 Hz). Electronic noise is added to each device according to its electrode area and empirical data with electrodes of that size. Ring electrodes (0.4 mm tall) had a noise value of 2.7 μV RMS. DISC had 96 electrodes each with an independent noise value of 4.3 μV RMS. Both noise values were randomly generated using a Gaussian distribution. The waveform and SNR calculations were made as follows:

$$w_{e,signal} = \sum_{s=1}^{8} source(t)_s + noise(t), \quad \text{(eq. 2)},$$

$$w_{e,noise} = \sum_{s=2}^{8} source(t)_s + noise(t), \quad \text{(eq. 3)},$$

$$SNR_s, dBV = 10\log\left[\frac{rms(\,w_{e,signal})}{rms(\,w_{e,noise})}\right], \quad \text{(eq. 4)},$$

where index *e* is specific to one electrode and device, and index *s* is specific to a source. Source amplitudes were sampled at the surface of the electrode. Source 1 in equations 2, 3 is by definition the primary or phase zero source. The primary source rotates for each of eight positions in Fig. 1A. SNR was computed for one cycle of the primary source.

The maximum amplitude of each source for each electrode and device type was computed by the ANSYS model as described before. The size and location of each source greatly influence the amplitude and noise contribution.

Suppl. Fig. 2 and Suppl. Movie 2 were a comparison of $Ø_{sh}$ = 70 and 800 μm. Dipoles were either parallel or orthogonal and varied of a gap distance of 0.15 to 5 mm. The “large dipole” source was 700-μm diameter.

2. Fabrication and assembly:

a. Microwires (Tetrode)

Eight insulated 12 nichrome microwires (PX27, Sandvik AB, Sweden) were folded at a length of 8 cm to make a compact bundle approximately 50-μm diameter. During recording, the four highest SNR electrodes were chosen. One end of the bundle was mounted and taped on an extended clamp arm, and a small weight was applied. While the taped end of the bundle was kept static, the other end was coiled vertically using a tetrode spinner (Neuralynx) for 35-40 turns.

A thin layer of medical grade epoxy (Epoxy 301, Epoxy Technology) was applied on the wire bundle to provide additional strength and rigidity towards implantation. Heat (250°F) was applied using a heat gun to cure the epoxy for 10 minutes. Tension was released from the coiled end and the bundle was allowed to untwist naturally. Post baking, both ends were cut with sharp scissors/ scalpel blades and the wire leads from the uncoiled end was manually connected to an Electrode Interface Board (Neuralynx EIB-36). The electrodes were electroplated in a gold non-cyanide solution (Neuralynx) within an ultrasonic bath using an AutoLab Electrochemical Workstation (Metrohm), until a nominal impedance (~250 kOhms) was achieved. The plated electrodes were cleaned with DI water, IPA and then air dried.

b. 128ch DISC

Planar 128-channel arrays (G-128, Diagnostic Biochips, Inc, Maryland, USA) made of polyimide (HD Microsystems PI2611) formed the electrode body. G-128 model has 200 μm and 250 μm vertical and horizontal pitch, respectively, and follows a 16x8 matrix (row x column) configuration. Each electrode was 80-μm in diameter and was coated with PEDOT. The thickness of the polyimide substrate with electrodes was approximately 12 μm. The planar electrode array was wrapped onto a guidewire/stylet using several techniques (Fig. 7A-C) to create a cylindrical lead body. Stainless steel (SS316) straight wire (GWXX-0170, 0.017” diameter, Component Supply Company) was used. To eliminate the possibility of the guidewire interfering with the electric field, PEBAX heat shrink tube (P2-023-0035-BLK, Cobalt Polymers, CA, USA) was applied on the SS wire. A 20-μm thick double coated acrylic tape (UTD-20B(W), Nitto, NJ, USA) was utilized to wrap the flexible electrode array on the PEBAX coated guidewire. A FusionPro 48 Laser machine (Epilog Laser, Golden, CO, USA) was employed to pattern the thin adhesive film so as to match the shape of the G-128 probe. The thin adhesive film was placed on a flat substrate and fixed each corner with tape. Then running under 60% of Speed, 6% of Power, and 70% of Frequency

with 2 cycles, the Vector mode from Laser machine could release desired adhesive film area within 20 seconds. Using a second heat shrink tube (PBST2-040-40-004C, Component Supply Company, USA), the electrode array was pressed firmly with the guidewire for better adhesion and to maintain the proper geometry. The guidewire tip was carefully machined to create a smooth insertion end for implantation with minimal blood vessel damage. Pre-implantation impedance was found to be (235 ± 244kΩ), while post implantation impedance was (432 kΩ ± 1.84MΩ).

3. Animal surgical procedure:

A total of 7 Sprague Dawley rats (250-450 gm) were used in this study. Rats were housed in pairs in a regular 12 h/12 h light/dark cycle with ad libitum access to food and water. All experimental procedures included analgesics and anesthesia and were approved by the Institutional Animal Care and Use Committee at Rice University. Rats were induced with 3-4% isoflurane (SomnoSuite, Kent Scientific) and all whiskers on the right facial pad were trimmed except B1, B2, C1, C2, D1, D2, E1, beta, delta, gamma, which were selected for stimulation. Subjects were mounted firmly with ear bars on a stereotactic frame (Harvard Apparatus). Lubricating eye gel was used to keep the animal eyes hydrated. Topical lidocaine gel was applied on the ear bars to reduce pain during mounting and subsequent processes. Meloxicam (5mg/ml) with a dose of 2mg/kg was injected SQ as an analgesic. Animal body heat was maintained with isothermal heating pads. Hair was trimmed, and post application of topical ethanol and betadine, a 2-3cm rostro caudal incision was made to expose the skull. Hydrogen peroxide was applied to clean excess tissue and periosteum, while electrocautery was applied to stop any unwanted bleeding. Anesthesia was maintained with 1-2% isoflurane during the surgery.

Using a micro burrs (FST, CA, US), a 4x4 mm^2 area of the skull was thinned on the left hemisphere. Brain images through the cranial window were captured with a CMOS sensor camera (CS126MU, Thorlabs, NJ, USA) mounted on a microscope (AmScope, CA, USA) using a 540nm light source to add contrast to the subdural vessels. Major blood vessels were avoided and a 900um twist drill hole was made near our estimated coordinates relative to bregma (C1 at -3.06 AP, 4.92 ML or D1 at -2.72 AP, 4.65 ML). These positions were adjusted proportionally for the nominal B-L distance of 8.8 mm. A stainless-steel bone screw (#0-80, Grainger, IL, USA) attached with a 32 AWG copper wire served as a reference electrode implanted above the cerebellum. The cranial burr hole was isolated using a layer of dental acrylic and silicone adhesive (Kwik-sil; World Precision Instruments, FL, USA), the reference electrode was isolated using dental acrylic only.

4. Electrophysiology recording protocol:

The whiskers were stimulated using a pneumatic dispenser (Nordson EFD Performus X, RI, USA). Each whisker was deflected by attaching a custom nozzle head to a standard 5mL syringe placed 2.5 mm from root of the whisker. The air puff (10 psi) from the nozzle head created a 10ms duration mechanical deflection in dorsal to ventral direction at 3 Hz over a 6s stimulus and 6s non-stimulus window; with a total of 450 stimulations recorded for each corresponding whisker. Neural signals from rat somatosensory cortex were recorded using our implanted set of microwire and DISC electrodes. Microwires were implanted at a depth of 1.4mm from the dura surface to collect large amplitude signals, while DISC implantation reached a depth of 3mm allowing the microelectrode array to be spanned over all cortical layers. Wideband signals were amplified, digitized and recorded using a 256 channels Intan RHD interface board (Intan Technology, CA, USA) using a sampling rate of 20,000 Hz. The whisker stimulation was driven by an Arduino which also read into digital port of the Intan recording system. The Arduino was operated on a lithium-ion battery source and recordings occurred in a faraday cage unless otherwise noted.

Neural signals were analyzed using offline custom Matlab scripts (Mathworks, MA, USA).

6. Data processing:

Raw neural signals were down sampled at 2 kHz, notch filtered at 60Hz, low-pass filtered (120 Hz, local field potential (LFP)), and band-pass filtered (40-150 Hz, Gamma band). To account for signal variability, LFP and Gamma signals were isolated for each trial. The signal amplitude was calculated by finding the distance between peak and valley poststimulation. The SNR was computed by dividing the root mean square (RMS) of the signal post-stimulation by RMS of the pre-stimulus baseline.

Directional curves (polar plots) are defined by the peak-to-peak LFP amplitude and electrode column. A unique column orientation was noted for each device we assembled relative to the plane of the PCB. The plane of the PCB was always implanted parallel to the coronal plane. This angular information was used in the generation of polar plots. We matched the electrode amplitude of the average waveform to its angle. If an electrode was missing, the cubic interpolation was performed. A 16-point cubic interpolation was made from 8 electrode columns assume equidistance between each column. Directional curves were standardized by subtracting the minimum amplitude.

Resultant vectors (RV) were calculated by the angle position of the electrode and the peak-to-peak LFP amplitude. The 8 original electrode positions were interpolated as described before to create 16 positions. The vectors were summed to create the resultant vector (length and angle).

A ring electrode was simulated by averaging the signal of the electrodes in the DISC array. The number of electrodes used for averaging was determined by the desired macroelectrode vertical length. For a 2 mm virtual macroelectrode, we used all the channels that were included in a 2 mm vertical span (11 rows) of the DISC array. For the 400 μm virtual macroelectrode, we used 2 adjacent rows of 8 microelectrodes each. The 0.4-mm rings were chosen to span supragranular, granular, and infragranular layers, assuming the granular layer included the transition to a negative evoked potential. The gap between each row was 400 μm.

We extracted the gamma band waveform from 0 to 100 ms poststimulation for each trial. The trial waveform from 44 electrodes, corresponding to 11 rows and 4 column, were concatenated into one matrix. This was defined as our feature matrix with columns as the gamma waveforms, and rows as individual trials. To reduce the dimensionality of our feature matrix, Principal Component Analysis (PCA) was performed, choosing the number of components necessary to represent the 99% variance of our data. The reduced feature matrix was then divided into 10-folds. Each fold used 80% for training and 20% for testing with a linear discriminant analysis (LDA) model.

By calculating the second derivative of the average LFP waveform, we computed the current source density (CSD, (Schroeder, Mehta, and Givre 1998)) of each DISC row. For optimal results, the 20,000 Hz sampling rate waveform was used.

7. Statistical analysis

Generalized Linear Mixed Model (GLMM) was used to study the differences of DISC device (intercept) compared to tetrode and virtual rings. The subjects were used as random effects, and SNR, amplitude and model accuracy as dependent variable. DISC was the defined baseline in the GLMM. When comparing between any two groups besides DISC, Tukey's range test was employed.

8. Perfusion and Histology:

A subset of rats had histology performed to identify the barrel location. Rats were euthanized by applying 5% isoflurane as a primary method, followed by cervical dislocation and thoracotomy as

a secondary method and confirmation, respectively. The subset prepared for histology were euthanized using 5% isoflurane and cervical dislocation, followed by transcardial perfusion of 2% PFA.

The cortex was flattened by scooping out the thalamus and placing in between two glass slides ~1.5mm apart. The flattened brain was kept in 1x PBS for 6-8 hours at 4°C. It was later transferred to a 2% PFA solution for 24 hours. Fixed flattened brain was washed with 0.1M 1X PBS and was sectioned using a vibratome (Leica VT 1200S, Germany) to create 50-80-µm slices. Sections were transferred to a culture plate culture plate and rinsed in Hepes buffer (0.1M pH 7.4) for 15 minutes. Cytochrome oxidase staining solution was prepared similar to [(Lauer et al. 2018)] and the sections were incubated in the solution at 37° C. Stains were visible around 30-60 mins. 2% PFA was added with the solution to stop the staining reaction. Sections were mounted on microscope glass slides and rinsed in consecutive 70% (2 mins), 96% (2 mins) and 99.5% (3 mins) ethanol. Sections were rinsed in isopropyl alcohol for 3 mins, followed by xylene rinse for 5 minutes to complete the dehydration process. Applying a non-aqueous mounting media, the sections were cover-slipped and imaged using a microscope (Keyence BZ-X800, Japan) and 20X objective. Electrode implantation location was reconstructed from the slides containing stained barrel cortex maps.

Acknowledgements

We would like to acknowledge John Mosher (UTHealth) for helpful discussions on source localization and dipole modeling. We thank the staff at Rice University's nanofabrication facility for supporting our neural probe development. We thank Charlie Schroeder for his insights into local field potential recording with varied devices. We acknowledge the Texas Institute of Restorative Neurotechnologies at UTHealth for its financial support.

Supplementary Information

Table of Contents

Suppl. Table 1. LDA Classification Accuracy by Device and Electrode Configuration

Suppl. Table 2. Source configuration table for a multi-source model (see Fig. 2).

Supp. Table 3. Electrical properties of electrostatic model.

Suppl. Fig. 1. 2D J-field and Voltage contour illustrating the mechanism of substrate shielding

Suppl. Fig. 2. Front/back amplitude by source type and orientation (related to Suppl. Movie 2)

Suppl. Fig. 3. SNR, amplitude, and noise comparison between a FEM ring and virtual DISC ring electrode.

Suppl. Fig. 4. *In vivo* performance of common average referencing (CAR).

Suppl. Fig. 5. Noise immunity with common average referencing (CAR)

Suppl. Fig. 6. Subject S6 histology and accuracy by whisker

Suppl. Movie 1: GIF of growing electrode size

Suppl. Movie 2: MP3 of monopole, dipole orientation

Suppl. Table 1. LDA Classification Accuracy by Device and Electrode Configuration

Device	Electrode Configuration (rows x columns)	Subject Accuracy							Average Accuracy
		S1	S2	S3	S4	S5	S6	S7	
DISC	11x8	92.6	98.5	98.2	96.0	92.4	93.3	91.5	94.7
	11x4	94.2	97.8	92.3	95.3	89.8	91.2	90.1	93.0
	3x8	92.9	97.2	84.8	93.8	89.2	88.2	86.9	90.4
	3x4	92.9	94.6	81.3	91.5	86.9	85.8	84.3	88.2
	1x4 (tetrode)	57.4	56.8	48.5	85.6	67.5	75.6	77.6	68.3
	Best 1	32.6	30.5	38.1	64.9	43.1	59.3	29.9	42.6
Tetrodes	Best 4	48.8	50.2	73.2	57.2	26.1	30.2	51.9	48.2
	Best 1	38.5	44.3	29.4	50.0	20.6	29.7	39.4	36.0
Virtual Macro	2 mm	24.6	42.1	36.7	74.1	22.8	40.3	25.8	38.1
	3 x 400 um	36.1	64.0	57.2	81.7	50.8	64.2	65.7	59.9

Suppl. Table 2. Source configuration table for a multi-source model (see Fig. 2).

Source number	Diameter, $Ø_{sh,\ \mu m}$	Gap distance, mm	Angle, degrees
1	200	1	0
2	400	3.16	19
3	200	0.6	94.4
4	800	5.12	107
5	400	1.73	190
6	800	4.63	212

7	1600	3.93	345
8	400	5.0	349

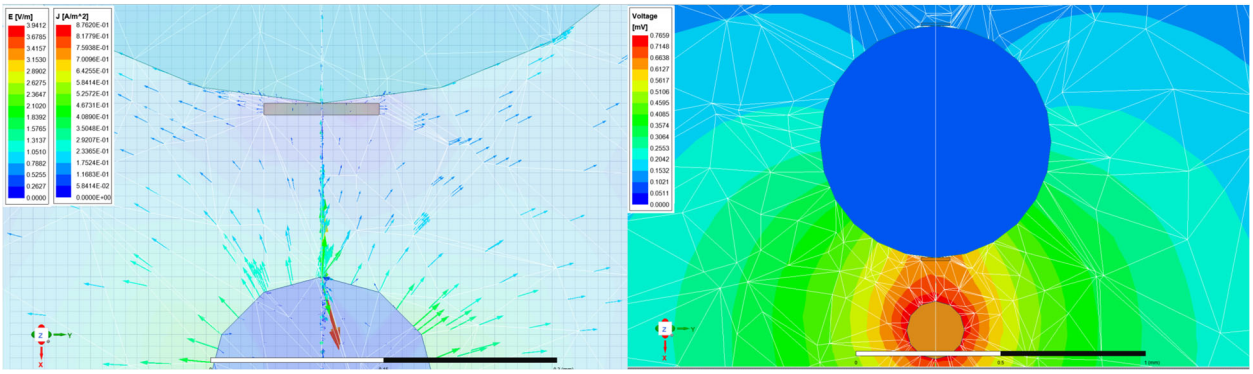

Suppl. Fig. 1: 2D J-field and Voltage contour illustrating the mechanism of substrate shielding. Top down view of a current field and potential contours around insulating bodies. The current vectors (left) illustrate the rapid divergence around the insulating body. The potential gradient (right) is steepest where the current magnitude is highest. The distance the isopotential extends away from the electrode toward the source is proportional to the size of the insulating body effectively decreasing the distance between electrode and source.

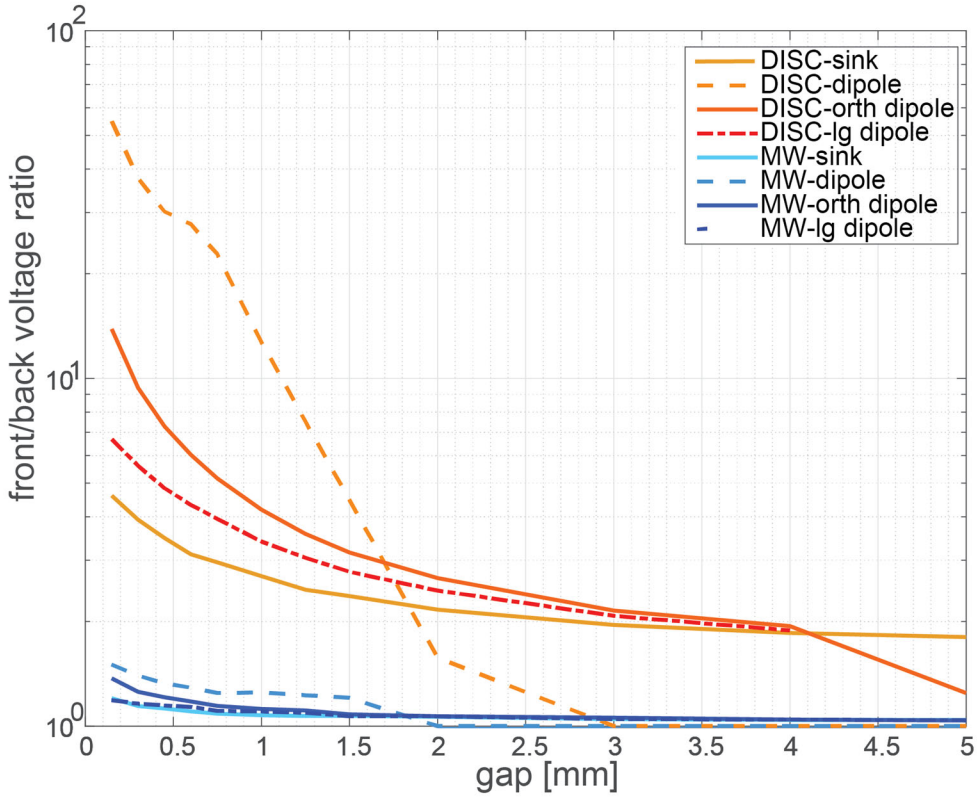

Suppl. Fig. 2. Front/back amplitude by source type and orientation (related to Suppl. Movie 2). FEM results for a 800-μm insulating body and a 200-μm dipole over a gap distance of 5 mm. The parallel-oriented dipole has the greatest directionality but the least range (3dB distance equals 1.9 mm). The monopole and orthogonal dipole performed similarly with a 3dB distance equal to 4.0 mm) (see also Suppl. Movie 2).

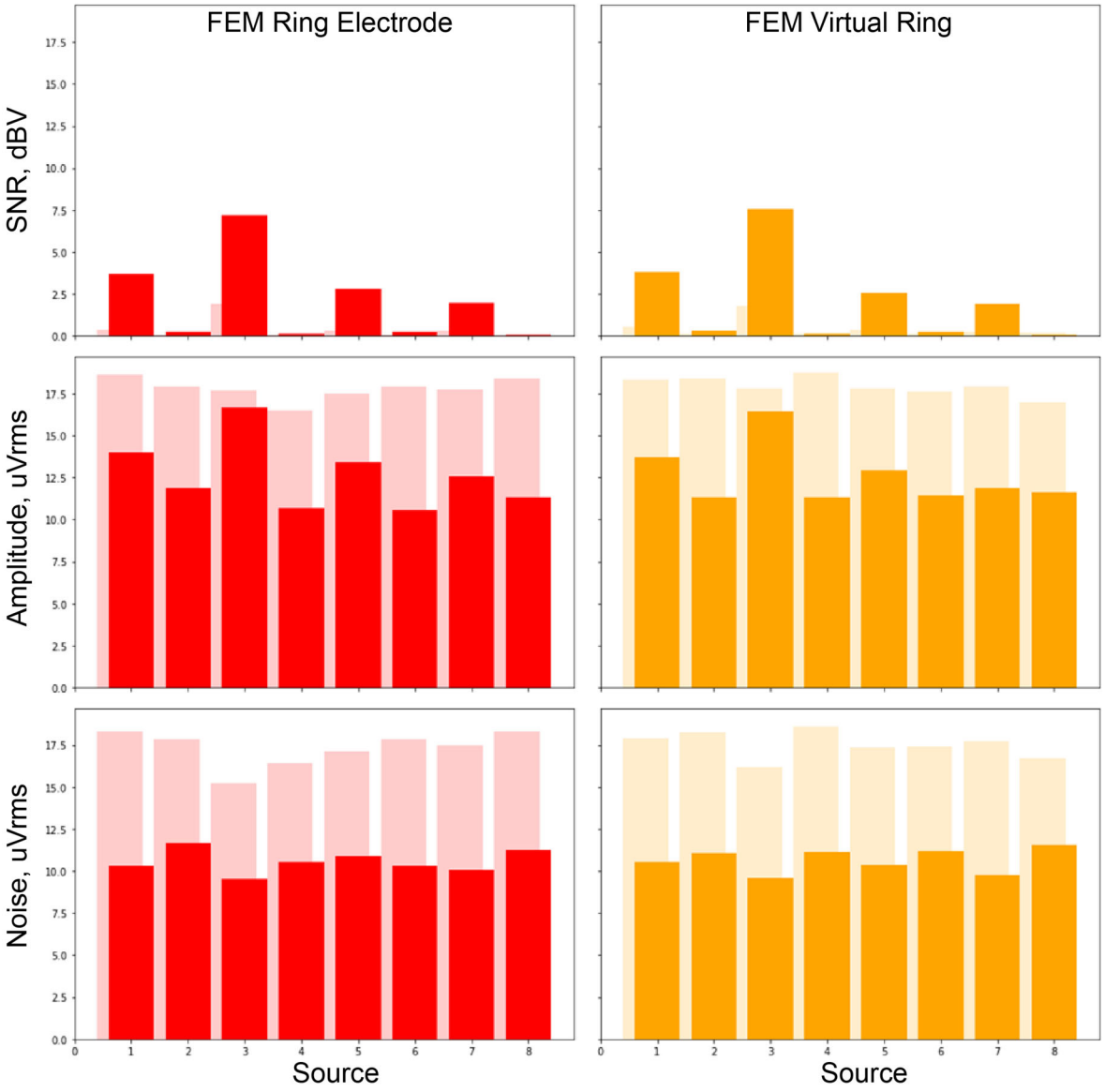

Suppl. Fig. 3. SNR, amplitude, and noise comparison between a FEM ring and virtual DISC ring electrode. An ANSYS model of a 0.4-mm tall ring electrode was tested in an 8 source environment (Fig. 2). This was compared with a 3 row, 8 column microelectrode array (200µm vertical pitch) in the same location then digitally averaged. The SNR, amplitude, and noise are separated for comparison. Light color represents one randomly seeded trial and dark color is the average after 50 trials. The ring was assigned 2.7 µVrms while each microelectrode was assigned 4.3 µVrms, which was the average noise floor values.

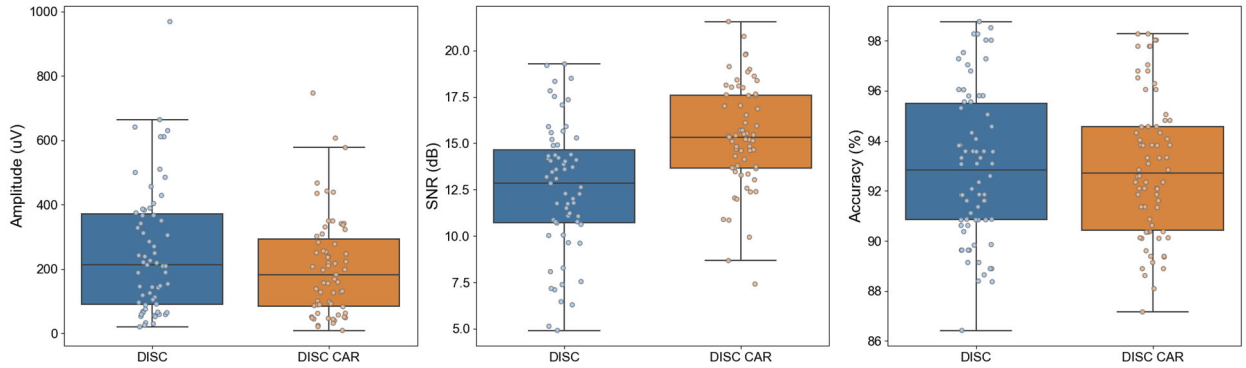

Suppl. Fig. 4. *In vivo* performance of common average referencing (CAR). Note that amplitude and SNR represent averages across each whisker, whereas accuracy is measured on a trial-by-trial basis. This may explain why SNR increased without improving accuracy but further investigation is required.

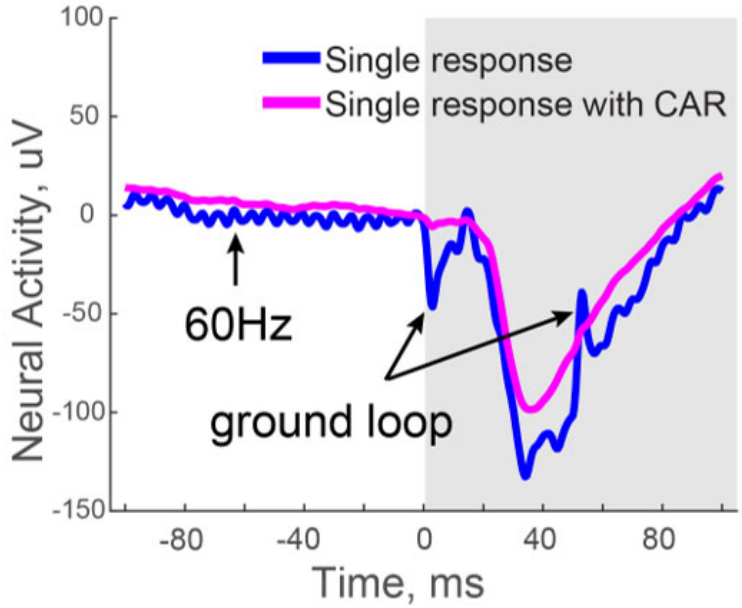

Suppl. Fig. 5. Noise immunity with common average referencing (CAR). Sample single trial of DISC in an *in vivo* stimulation trial without the use of a Faraday cage. The ground loop was intentionally created by connecting the air puffer ground at a separate outlet. Both signals were identically filtered. CAR effectively removes common mode noise with a small decrease in the evoked potential.

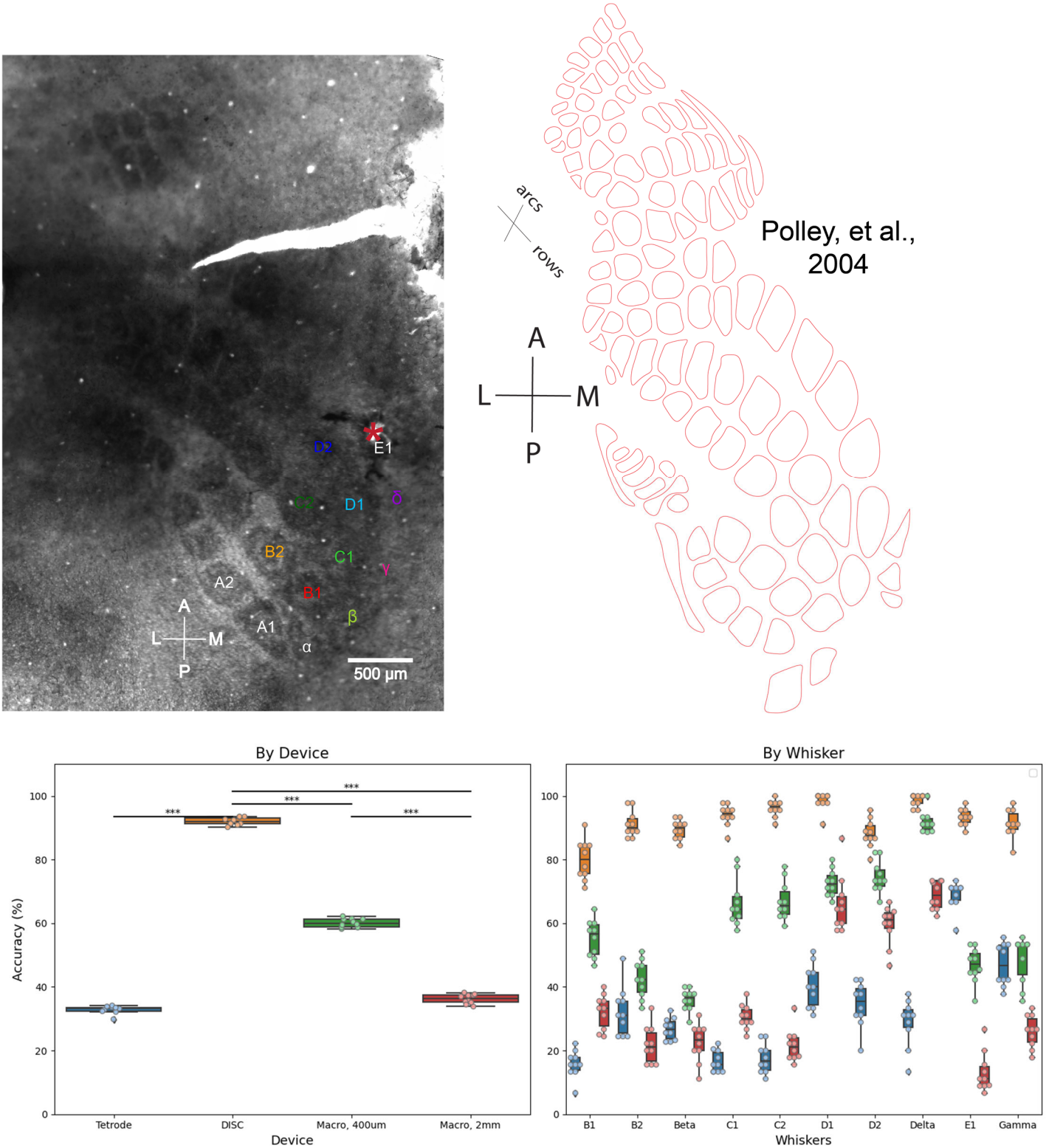

Suppl. Fig. 6. Subject S6 histology and accuracy by whisker. The position of the implant was barrel E1. A useful reference for identifying barrels in rats is Polley et al. (Polley, Kvašňák, and

Frostig 2004). Further evidence of implanting in E1 was the tetrode amplitude, which was maximum at E1 (data not shown). DISC performed well in classification across the whiskers despite a maximum distance of 1.45 mm. Also promising is the overall performance even though most sources were positioned at roughly the same angle from DISC.

Bibliography

Anderson, David J, Karim G Oweiss, and Steven M Bierer. 2001. “Sensor Arrays in the Micro-Environment of the Brain.” In *Acoustics, Speech, and Signal Processing, 2001. Proceedings.(ICASSP’01). 2001 IEEE International Conference On*, 6:3433–36. IEEE.

Angrick, M., M. Ottenhoff, L. Diener, D. Ivucic, G. Ivucic, S. Goulis, J. Saal, et al. 2020. “Real-Time Synthesis of Imagined Speech Processes from Minimally Invasive Recordings of Neural Activity.” *BioRxiv*, no. 2. https://doi.org/10.1101/2020.12.11.421149.

Baillet, Sylvain, John C Mosher, and Richard M Leahy. 2001. “Electromagnetic Brain Mapping.” *IEEE Signal Processing Magazine* 18 (6): 14–30.

Bancaud, Jean, Jean Talairach, A Bonis, C Schaub, G Szikla, P Morel, and M Bordas-Ferrer. 1965. “La Stéreoencephalographie Dans l’épilepsie.” *Mattson, Paris*, 113–46.

Blanche, Timothy J, Martin A Spacek, Jamille F Hetke, and Nicholas V Swindale. 2005. “Polytrodes: High-Density Silicon Electrode Arrays for Large-Scale Multiunit Recording.” *Journal of Neurophysiology* 93 (5): 2987–3000.

Bullard, Autumn J., Brianna C. Hutchison, Jiseon Lee, Cynthia A. Chestek, and Parag G. Patil. 2020. “Estimating Risk for Future Intracranial, Fully Implanted, Modular Neuroprosthetic Systems: A Systematic Review of Hardware Complications in Clinical Deep Brain Stimulation and Experimental Human Intracortical Arrays.” *Neuromodulation* 23 (4): 411–26. https://doi.org/10.1111/ner.13069.

Buzsáki, György, Costas A. Anastassiou, and Christof Koch. 2012. “The Origin of Extracellular Fields and Currents-EEG, ECoG, LFP and Spikes.” *Nature Reviews Neuroscience* 13 (6): 407–20. https://doi.org/10.1038/nrn3241.

Du, Jiangang, Michael L Roukes, and Sotiris C Masmanidis. 2009. “Dual-Side and Three-Dimensional Microelectrode Arrays Fabricated from Ultra-Thin Silicon Substrates.” *Journal*

of Micromechanics and Microengineering 19 (7): 75008.

Dura-Bernal, Salvador, Benjamin A. Suter, Padraig Gleeson, Matteo Cantarelli, Adrian Quintana, Facundo Rodriguez, David J. Kedziora, et al. 2019. “NetpyNE, a Tool for Data-Driven Multiscale Modeling of Brain Circuits.” *ELife* 8: 1–26. https://doi.org/10.7554/eLife.44494.

Engel, Jerome. 2018. “The Current Place of Epilepsy Surgery.” *Current Opinion in Neurology* 31 (2): 192–97. https://doi.org/10.1097/WCO.0000000000000528.

Flint, Robert D, Zachary A Wright, Michael R Scheid, and Marc W Slutzky. 2013. “Long Term, Stable Brain Machine Interface Performance Using Local Field Potentials and Multiunit Spikes.” *Journal of Neural Engineering* 10 (5): 56005.

Fried, Itzhak, Charles L. Wilson, Nigel T. Maidment, Jerome Engel, Eric Behnke, Tony A. Fields, Katherine A. Macdonald, Jack W. Morrow, and Larry Ackerson. 1999. “Cerebral Microdialysis Combined with Single-Neuron and Electroencephalographic Recording in Neurosurgical Patients: Technical Note.” *Journal of Neurosurgery* 91 (4): 697–705. https://doi.org/10.3171/jns.1999.91.4.0697.

Gerbella, M., E. Borra, F. Pothof, M. Lanzilotto, A. Livi, L. Fogassi, O. Paul, G. A. Orban, P. Ruther, and L. Bonini. 2021. “Histological Assessment of a Chronically Implanted Cylindrically-Shaped, Polymer-Based Neural Probe in the Monkey.” *Journal of Neural Engineering* 18 (2). https://doi.org/10.1088/1741-2552/abdd11.

Hagen, Espen, Solveig Næss, Torbjørn V. Ness, and Gaute T. Einevoll. 2018. “Multimodal Modeling of Neural Network Activity: Computing LFP, ECoG, EEG, and MEG Signals with LFPy 2.0.” *Frontiers in Neuroinformatics* 12 (December). https://doi.org/10.3389/fninf.2018.00092.

Hämäläinen, Matti, Riitta Hari, Risto J Ilmoniemi, Jukka Knuutila, and Olli V Lounasmaa. 1993. “Magnetoencephalography—Theory, Instrumentation, and Applications to Noninvasive Studies of the Working Human Brain.” *Reviews of Modern Physics* 65 (2): 413.

Hammer, Jiří, Tobias Pistohl, Jörg Fischer, Pavel Kršek, Martin Tomášek, Petr Marusič, Andreas Schulze-Bonhage, Ad Aertsen, and Tonio Ball. 2016. “Predominance of Movement Speed over Direction in Neuronal Population Signals of Motor Cortex: Intracranial EEG Data and A Simple Explanatory Model.” *Cerebral Cortex* 26 (6): 2863–81. https://doi.org/10.1093/cercor/bhw033.

Hanalioglu, Sahin, Gokhan Bozkurt, Ilkay Isikay, and Orkhan Mammadkhanli. 2020. “A Simple

and Effective Modified Technique of Twist Drill Craniostomy for Bedside Drainage and Irrigation of Chronic Subdural Hematoma: Technical and Clinical Study." *Clinical Neurology and Neurosurgery* 199: 106262.

Herff, Christian, Dean J. Krusienski, and Pieter Kubben. 2020. "The Potential of Stereotactic-EEG for Brain-Computer Interfaces: Current Progress and Future Directions." *Frontiers in Neuroscience* 14 (February): 1–8. https://doi.org/10.3389/fnins.2020.00123.

Herreras, Oscar. 2016. "Local Field Potentials: Myths and Misunderstandings." *Frontiers in Neural Circuits* 10 (DEC): 1–16. https://doi.org/10.3389/fncir.2016.00101.

Hochberg, Leigh R, Daniel Bacher, Beata Jarosiewicz, Nicolas Y Masse, John D Simeral, Joern Vogel, Sami Haddadin, Jie Liu, Sydney S Cash, and Patrick van der Smagt. 2012. "Reach and Grasp by People with Tetraplegia Using a Neurally Controlled Robotic Arm." *Nature* 485 (7398): 372–75.

Jun, James J, Nicholas A Steinmetz, Joshua H Siegle, Daniel J Denman, Marius Bauza, Brian Barbarits, Albert K Lee, Costas A Anastassiou, Alexandru Andrei, and Çağatay Aydın. 2017. "Fully Integrated Silicon Probes for High-Density Recording of Neural Activity." *Nature* 551 (7679): 232.

Kaiboriboon, Kitti, Ayham M Malkhachroum, Ahmad Zrik, Ahmad Daif, Nicholas M Schiltz, David M Labiner, and Samden D Lhatoo. 2015. "Epilepsy Surgery in the United States: Analysis of Data from the National Association of Epilepsy Centers." *Epilepsy Research* 116: 105–9.

Kajikawa, Yoshinao, and Charles E. Schroeder. 2011. "How Local Is the Local Field Potential?" *Neuron* 72 (5): 847–58. https://doi.org/10.1016/j.neuron.2011.09.029.

Kajikawa, Yoshinao, and Charles E. Schroeder. 2015. "Generation of Field Potentials and Modulation of Their Dynamics through Volume Integration of Cortical Activity." *Journal of Neurophysiology* 113 (1): 339–51. https://doi.org/10.1152/jn.00914.2013.

Kato, Hiroyuki K, Samuel K Asinof, and Jeffry S Isaacson. 2017. "Network-Level Control of Frequency Tuning in Auditory Cortex." *Neuron* 95 (2): 412–23.

Koessler, Laurent, Sophie Colnat-Coulbois, Thierry Cecchin, Janis Hofmanis, Jacek P Dmochowski, Anthony M Norcia, and Louis G Maillard. 2017. "In-vivo Measurements of Human Brain Tissue Conductivity Using Focal Electrical Current Injection through Intracerebral Multicontact Electrodes." *Human Brain Mapping* 38 (2): 974–86.

Kovac, Stjepana, Vejay N Vakharia, Catherine Scott, and Beate Diehl. 2017. "Invasive Epilepsy

Surgery Evaluation." *Seizure* 44: 125–36.

Lauer, Simon M, Undine Schneeweiß, Michael Brecht, and Saikat Ray. 2018. "Visualization of Cortical Modules in Flattened Mammalian Cortices." *Journal of Visualized Experiments: JoVE*, no. 131.

Lindén, Henrik, Tom Tetzlaff, Tobias C. Potjans, Klas H. Pettersen, Sonja Grün, Markus Diesmann, and Gaute T. Einevoll. 2011. "Modeling the Spatial Reach of the LFP." *Neuron* 72 (5): 859–72. https://doi.org/10.1016/j.neuron.2011.11.006.

Luan, Lan, Xiaoling Wei, Zhengtuo Zhao, Jennifer J. Siegel, Ojas Potnis, Catherine A. Tuppen, Shengqing Lin, et al. 2017. "Ultraflexible Nanoelectronic Probes Form Reliable, Glial Scar–Free Neural Integration." *Science Advances* 3 (2): 1–10. https://doi.org/10.1126/sciadv.1601966.

Lucka, Felix, Sampsa Pursiainen, Martin Burger, and Carsten H Wolters. 2012. "Hierarchical Bayesian Inference for the EEG Inverse Problem Using Realistic FE Head Models: Depth Localization and Source Separation for Focal Primary Currents." *NeuroImage* 61 (4): 1364–82.

Ludwig, Kip A, Rachel M Miriani, Nicholas B Langhals, Michael D Joseph, David J Anderson, and Daryl R Kipke. 2009. "Using a Common Average Reference to Improve Cortical Neuron Recordings from Microelectrode Arrays." *Journal of Neurophysiology* 101: 1679–89. https://doi.org/10.1152/jn.90989.2008.

Makin, Joseph G, David A Moses, and Edward F Chang. 2020. "With an Encoder – Decoder Framework." *Nature Neuroscience* 23 (4): 575–82. https://doi.org/10.1038/s41593-020-0608-8.

Moffitt, Michael A, and Cameron C McIntyre. 2005. "Model-Based Analysis of Cortical Recording with Silicon Microelectrodes." *Clinical Neurophysiology* 116 (9): 2240–50.

Moses, David A., Sean L. Metzger, Jessie R. Liu, Gopala K. Anumanchipalli, Joseph G. Makin, Pengfei F. Sun, Josh Chartier, et al. 2021. "Neuroprosthesis for Decoding Speech in a Paralyzed Person with Anarthria." *New England Journal of Medicine* 385 (3): 217–27. https://doi.org/10.1056/nejmoa2027540.

Murakami, Shingo, and Yoshio Okada. 2015. "NeuroImage Invariance in Current Dipole Moment Density across Brain Structures and Species : Physiological Constraint for Neuroimaging." *NeuroImage* 111: 49–58. https://doi.org/10.1016/j.neuroimage.2015.02.003.

Na, Kyounghwan, Zachariah J Sperry, Jiaao Lu, Mihaly Voeroeslakos, Saman S Parizi, Tim M Bruns, Euisik Yoon, and John P Seymour. “Novel Diamond Shuttle to Deliver Flexible Bioelectronics with Reduced Tissue Compression.” *Microsystems & Nanoengineering*, January. http://biorxiv.org/content/early/2018/10/17/435800.abstract.

Næss, Solveig, Geir Halnes, Espen Hagen, Donald J Hagler, Anders M Dale, Gaute T Einevoll, and Torbjørn V Ness. 2021. “Biophysically Detailed Forward Modeling of the Neural Origin of EEG and MEG Signals.” *NeuroImage* 225 (September 2020): 117467. https://doi.org/10.1016/j.neuroimage.2020.117467.

Neymotin, Samuel A., Dylan S. Daniels, Blake Caldwell, Robert A. McDougal, Nicholas T. Carnevale, Mainak Jas, Christopher I. Moore, Michael L. Hines, Matti Hämäläinen, and Stephanie R. Jones. 2020. “Human Neocortical Neurosolver (HNN), a New Software Tool for Interpreting the Cellular and Network Origin of Human MEG/EEG Data.” *ELife* 9: 1–39. https://doi.org/10.7554/eLife.51214.

Noor, M Sohail, and Cameron C Mcintyre. 2021. “Biophysical Characterization of Local Field Potential Recordings from Directional Deep Brain Stimulation Electrodes.” *Clinical Neurophysiology*. https://doi.org/10.1016/j.clinph.2021.01.027.

Nunez, Paul L., and Ramesh Srinivasan. 2010. “Scale and Frequency Chauvinism in Brain Dynamics: Too Much Emphasis on Gamma Band Oscillations.” *Brain Structure and Function* 215 (2): 67–71. https://doi.org/10.1007/s00429-010-0277-6.

Nunez, Paul L, Michael D Nunez, and Ramesh Srinivasan. 2019. “Multi-Scale Neural Sources of EEG : Genuine , Equivalent , and Representative . A Tutorial Review.” *Brain Topography* 32 (2): 193–214. https://doi.org/10.1007/s10548-019-00701-3.

Nunez, Paul L, and Ramesh Srinivasan. 2006. *Electric Fields of the Brain: The Neurophysics of EEG*. Oxford University Press, USA.

Oosugi, Naoya, Keiichi Kitajo, Naomi Hasegawa, Yasuo Nagasaka, Kazuo Okanoya, and Naotaka Fujii. 2017. “A New Method for Quantifying the Performance of EEG Blind Source Separation Algorithms by Referencing a Simultaneously Recorded ECoG Signal.” *Neural Networks* 93: 1–6.

Perge, János A., Shaomin Zhang, Wasim Q. Malik, Mark L. Homer, Sydney Cash, Gerhard Friehs, Emad N. Eskandar, John P. Donoghue, and Leigh R. Hochberg. 2014. “Reliability of Directional Information in Unsorted Spikes and Local Field Potentials Recorded in Human

Motor Cortex." *Journal of Neural Engineering* 11 (4). https://doi.org/10.1088/1741-2560/11/4/046007.

Peron, Simon P., Jeremy Freeman, Vijay Iyer, Caiying Guo, and Karel Svoboda. 2015. "A Cellular Resolution Map of Barrel Cortex Activity during Tactile Behavior." *Neuron* 86 (3): 783–99. https://doi.org/10.1016/j.neuron.2015.03.027.

Pesaran, Bijan, Martin Vinck, Gaute T. Einevoll, Anton Sirota, Pascal Fries, Markus Siegel, Wilson Truccolo, Charles E. Schroeder, and Ramesh Srinivasan. 2018. "Investigating Large-Scale Brain Dynamics Using Field Potential Recordings: Analysis and Interpretation." *Nature Neuroscience* 21 (7): 903–19. https://doi.org/10.1038/s41593-018-0171-8.

Petersen, Carl C.H. 2019. "Sensorimotor Processing in the Rodent Barrel Cortex." *Nature Reviews Neuroscience* 20 (9): 533–46. https://doi.org/10.1038/s41583-019-0200-y.

Polley, Daniel B., Eugen Kvašňák, and Ron D. Frostig. 2004. "Naturalistic Experience Transforms Sensory Maps in the Adult Cortex of Caged Animals." *Nature* 429 (6987): 67–71. https://doi.org/10.1038/nature02469.

Pothof, F., L. Bonini, M. Lanzilotto, A. Livi, L. Fogassi, G. A. Orban, O. Paul, and P. Ruther. 2016. "Chronic Neural Probe for Simultaneous Recording of Single-Unit, Multi-Unit, and Local Field Potential Activity from Multiple Brain Sites." *Journal of Neural Engineering* 13 (4): 1–13. https://doi.org/10.1088/1741-2560/13/4/046006.

Rollo, Patrick S., Matthew J. Rollo, Ping Zhu, Oscar Woolnough, and Nitin Tandon. 2021. "Oblique Trajectory Angles in Robotic Stereoelectroencephalography." *Journal of Neurosurgery* 135 (1): 245–54. https://doi.org/10.3171/2020.5.JNS20975.

Sacino, Matthew F., Sean S. Huang, John Schreiber, William D. Gaillard, and Chima O. Oluigbo. 2019. "Is the Use of Stereotactic Electroencephalography Safe and Effective in Children? A Meta-Analysis of the Use of Stereotactic Electroencephalography in Comparison to Subdural Grids for Invasive Epilepsy Monitoring in Pediatric Subjects." *Clinical Neurosurgery*. https://doi.org/10.1093/neuros/nyy466.

Schroeder, Charles E, Ashesh D Mehta, and Syndee J Givre. 1998. "A Spatiotemporal Profile of Visual System Activation Revealed by Current Source Density Analysis in the Awake Macaque." *Cerebral Cortex (New York, NY: 1991)* 8 (7): 575–92.

Seymour, John P, Nick B Langhals, David J Anderson, and Daryl R Kipke. 2011. "Novel Multi-Sided, Microelectrode Arrays for Implantable Neural Applications." *Biomedical Microdevices*

13 (3): 441–51.

Shannon, Claude Elwood. 1948. “A Mathematical Theory of Communication.” *The Bell System Technical Journal* 27 (3): 379–423.

Tadel, François, Sylvain Baillet, John C Mosher, Dimitrios Pantazis, and Richard M Leahy. 2011. “Brainstorm: A User-Friendly Application for MEG/EEG Analysis.” *Computational Intelligence and Neuroscience* 2011.

Tandon, Nitin, BA Tong, ER Friedman, JA Johnson, G Von Allmen, MS Thomas, OA Hope, Giridhar P. Kalamangalam, Jeremy D. Slater, and Thompson SA. 2019. “Analysis of Morbidity and Outcomes Associated With Use of Subdural Grids vs Stereoelectroencephalography in Patients With Intractable Epilepsy.” *JAMA Neurol.*

Tandon, Nitin, Brian A Tong, Elliott R Friedman, Jessica A Johnson, Gretchen Von Allmen, Melissa S Thomas, Omotola A Hope, Giridhar P Kalamangalam, Jeremy D Slater, and Stephen A Thompson. 2019. “Analysis of Morbidity and Outcomes Associated with Use of Subdural Grids vs Stereoelectroencephalography in Patients with Intractable Epilepsy.” *JAMA Neurology* 76 (6): 672–81.

Thomas, Tessy M, Robert W Nickl, Margaret C Thompson, Daniel N Candrea, Matthew S Fifer, David P McMullen, Luke E Osborn, Eric A Pohlmeyer, Manuel Anaya, and William S Anderson. 2020. “Simultaneous Classification of Bilateral Hand Gestures Using Bilateral Microelectrode Recordings in a Tetraplegic Patient.” *MedRxiv*.

Toth, Marton, Kata Szilvia Papp, Noemi Gede, Kornelia Farkas, Sandor Kovacs, Jean Isnard, Koichi Hagiwara, et al. 2019. “Surgical Outcomes Related to Invasive EEG Monitoring with Subdural Grids or Depth Electrodes in Adults: A Systematic Review and Meta-Analysis.” *Seizure*. https://doi.org/10.1016/j.seizure.2019.06.022.

Ulbert, István, Eric Halgren, Gary Heit, and George Karmos. 2001. “Multiple Microelectrode-Recording System for Human Intracortical Applications.” *Journal of Neuroscience Methods* 106 (1): 69–79. https://doi.org/10.1016/S0165-0270(01)00330-2.

Vakharia, Vejay N, Rachel Sparks, Aidan G O’Keeffe, Roman Rodionov, Anna Miserocchi, Andrew McEvoy, Sebastien Ourselin, and John Duncan. 2017. “Accuracy of Intracranial Electrode Placement for Stereoelectroencephalography: A Systematic Review and Meta-analysis.” *Epilepsia* 58 (6): 921–32.

Wellman, Steven M, James R Eles, Kip A Ludwig, John P Seymour, Nicholas J Michelson, William

E McFadden, Alberto L Vazquez, and Takashi D Y Kozai. 2017. “A Materials Roadmap to Functional Neural Interface Design.” *Advanced Functional Materials*.

Willett, Francis R, Donald T Avansino, Leigh R Hochberg, Jaimie M Henderson, and Krishna V Shenoy. n.d. “High-Performance Brain-to-Text Communication via Imagined Handwriting 1 2.” https://doi.org/10.1101/2020.07.01.183384.

Xu, Changsong, Bing Chen, Liujun Xue, Lei Xia, Xiu Yang, Ming Wei, Xiaobo Hui, Quan Chen, Jinlong Zheng, and Zhengming Li. 2018. “Randomized Controlled Study on the Curative Effects of Twist-drill Craniotomy and Burr-hole Craniotomy in the Treatment of Chronic Subdural Hematoma.” *Experimental and Therapeutic Medicine* 16 (2): 959–65.

Yan, Han, Joel S. Katz, Melanie Anderson, Alireza Mansouri, Madison Remick, George M. Ibrahim, and Taylor J. Abel. 2019. “Method of Invasive Monitoring in Epilepsy Surgery and Seizure Freedom and Morbidity: A Systematic Review.” *Epilepsia*. https://doi.org/10.1111/epi.16315.

Yang, Meihua, Yuanshi Ma, Wei Li, Xianjun Shi, Zhi Hou, Ning An, Chunqing Zhang, Lihong Liu, Hui Yang, and Dong Zhang. 2017. “A Retrospective Analysis of Stereoelectroencephalography and Subdural Electroencephalography for Preoperative Evaluation of Intractable Epilepsy.” *Stereotactic and Functional Neurosurgery* 95 (1): 13–20.